

SPACE SCIENCES

Assessing the global Alfvén wave power flow into and out of the auroral acceleration region during geomagnetic storms

Andreas Keiling^{1*}, Scott Thaller^{2†}, John Wygant², John Dombeck²

Geomagnetic storms are large space weather events with potentially tremendous societal implications. During these storms, the transfer of energy from the solar wind into geospace is largely increased, leading to enhanced energy flow and deposition within the magnetosphere and ionosphere. While various energy forms participate, the rate of total Alfvén wave energy flowing into the auroral acceleration region—where the magnetosphere and ionosphere couple—has not been quantified. Here, we report a fourfold increase in hemispherical Alfvénic power (from 2.59 to 10.05 GW) over a largely expanded oval band covering all longitudes and latitudes between 50° and 85° during the main storm phase compared with nonstorm periods. The Poynting flux associated with individual Alfvén waves reached values of up to about 0.5 W/m² (mapped to ionospheric altitude). These results demonstrate that Alfvén waves are an important component of geomagnetic storms and associated energy flow into the auroral acceleration region.

INTRODUCTION

How geomagnetic storms affect our planet and the near-Earth space environment (geospace) is one of the most important and pertinent aspects of space weather research (1). Geomagnetic storms lead to increased energy input into geospace followed by enhanced energy flow and deposition within it. While the energy originates in coronal mass ejections (CMEs) on the Sun's surface, the encounter of a CME with Earth's magnetosphere leads to a myriad of phenomena, which are collectively known as a geomagnetic storm [see review by (2)] and will hereafter be called storm for brevity. One of the most obvious phenomena, because it is visible to the human eye, is enhanced aurora. Since the 19th century, “grand” auroras—more global, more intense—have been related to increased disturbances in the geomagnetic field [e.g., (3)]. As an example of a storm aurora, Fig. 1A shows the initial auroral development of a storm. In addition to beautiful auroras, it is now known that much is at stake during times of intense geomagnetic storms, namely, the disruption and destruction of technological systems (4). Hence, there exists a societal necessity to study this space weather phenomenon.

Energy transfer and deposition are central to the study of storms and the coupled solar wind–magnetosphere–ionosphere system. Various modes of energy transfer and energy sinks during storms have been identified [see (2) for a review]. Ultimately, the polar ionosphere is the last region in this coupled system (excluding plasmoids, which are ejected into the solar wind) where storm energy is deposited in the form of Joule heating and particle precipitation (part of which causes auroral luminosity). While the polar ionosphere largely acts as a load (but not exclusively) in the auroral current circuit, this circuit also includes the magnetospheric generator (or generators) and the so-called auroral acceleration region (AAR) (Fig. 1B). The AAR appears to be a necessary transition region between a collisionless

and tenuous magnetospheric plasma and a collisional and dense ionospheric plasma. This coupling also exists at other astronomical bodies, such as other planets and the Sun [e.g., see review by (5)]. In the case of Earth, the AAR encircles both poles in an oval shape with an upper limit that approximately extends to 3.5 RE, measured from the center of Earth (1 RE = 1 Earth radius) [see review by (6)]. It is a major region for energy conversion processes; in particular, inflowing electromagnetic energy is converted into the kinetic energy of electrons and ions—hence its name.

In recent years, it has been shown that Alfvén waves are important carriers of energy in the auroral current circuit during dynamic space weather events [e.g., (7, 8), and for a review see (9)]. It is also known that the equatorial magnetospheric regions—both dayside and nightside—and the distant magnetotail are regions of Alfvén wave generation [e.g., (10, 11)]. The Alfvénic electromagnetic energy (Poynting flux) coming from the remote generator regions is funneled along magnetic field lines toward the top of the AAR, forming the narrower end of a gigantic “magnetic funnel” (Fig. 1C). By carrying energy into the AAR, the waves then trigger other processes at lower altitudes, most notably the acceleration of electrons, which precipitate into the ionosphere, where they contribute to the aurora [see review by (12)]. However, the top side of the AAR is an unexpectedly unexplored region with regard to storm Alfvén waves. To assess their impact during storms, in this study we quantify the electromagnetic energy rate (power) with which Alfvén waves enter and leave the entire AAR and show how this power is distributed along the oval-shaped AAR. This will also allow us to make comparisons with energy carriers exiting the AAR at the bottom, such as auroral electrons and Alfvén waves. These results will provide a missing link in the global energy budget of storms.

RESULTS

To assess the global energy flow of magnetohydrodynamic (MHD) Alfvén waves (see Materials and Methods for a discussion on the MHD regime versus the kinetic regime) into and out of the AAR during storms, we focused on the 23rd solar cycle, which started in

Copyright © 2019
The Authors, some
rights reserved;
exclusive licensee
American Association
for the Advancement
of Science. No claim to
original U.S. Government
Works. Distributed
under a Creative
Commons Attribution
NonCommercial
License 4.0 (CC BY-NC).

¹Space Sciences Laboratory, University of California at Berkeley, Berkeley, CA, USA.

²University of Minnesota, Minneapolis, MN, USA.

*Corresponding author. Email: keiling@berkeley.edu

†Present address: Laboratory for Atmospheric and Space Physics, University of Colorado Boulder, Boulder, CO, USA.

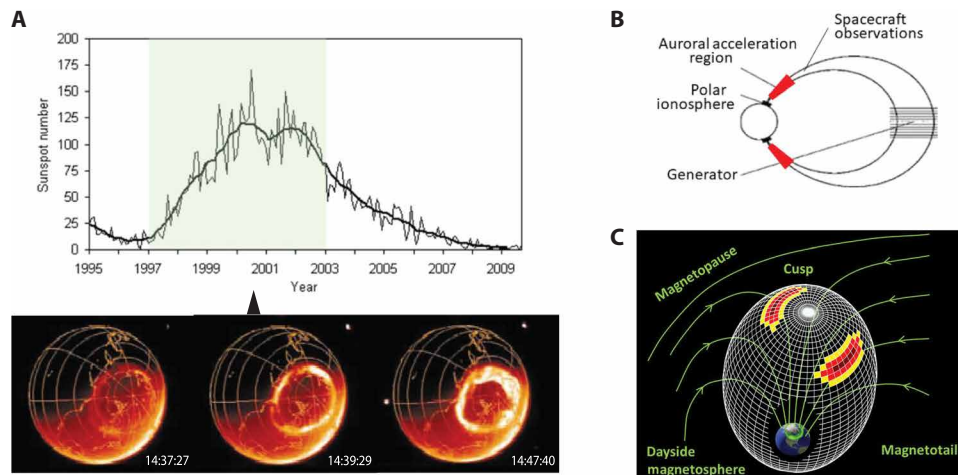


Fig. 1. Solar cycle and experimental setup. (A) Top: Sunspot number versus time. The period under investigation in this study is shaded green, and the thick line is the averaged curve. Bottom: Global view of the initial development of the aurora during the Bastille Day storm observed by the IMAGE spacecraft's Wideband Imaging Camera [from (4)]. The time in the lower right-hand corner of each image is in universal time. The arrow above the three images points at the date in the solar cycle when this storm occurred. (B) Auroral current circuit with key regions and spacecraft location [modified from (60)]. (C) Hypothetical orbital ellipsoid of the Polar satellite crossing different plasma regions of Earth's magnetosphere during 1 year. The colored regions (yellow and red) illustrate regions through which Alfvén waves travel toward or away from the ionosphere in one particular instance. The hole in the ellipsoid reveals Earth with the aurora borealis. Green lines with arrows represent magnetic field lines.

September 1996. Six complete years of data from the Polar satellite (from 1997 to 2002) were used, which is about half the solar cycle, including one minimum and one maximum of sunspot counts (Fig. 1A). Typically, during a solar cycle, the number of storm occurrences increases around the peak and the subsequent decline of the sunspot counts. During the 6-year period, the satellite traversed magnetic field lines at 4 to 7 RE (i.e., above the AAR) in the Northern Hemisphere, allowing calculations of the total Alfvénic power before entering the AAR. The global spatial distribution of the Poynting flux in the Northern Hemisphere—averaged over the 6 years—flowing through the orbital ellipsoid (Fig. 1C) and projected along magnetic field lines to ionospheric altitude (100 km) is shown in Fig. 2 (A and C) for nonstorm periods and in Fig. 2 (B and D) for storm periods (see Materials and Methods for a description of how the figure was produced). We used the common disturbance storm time (Dst) index with values less than 0 nT and greater than -20 nT for nonstorm periods and less than -40 nT for storm periods. It is apparent that there are notable differences between the nonstorm and storm distributions. Overall, the global “band” of more intense Alfvén wave activity is substantially increased in size during storm periods, compared with that of nonstorm periods. This global broadening results in an increase from 2.6 to 8.6 GW (indicated in the lower left of Fig. 2, A and B) of the total integrated hemispherical powers flowing into the AAR (i.e., downward). In contrast, there is much less Alfvén wave activity and total integrated power flowing out of the AAR (i.e., upward) during both nonstorm periods (Fig. 2C) and storm periods (Fig. 2D). The proportion of outflowing power with respect to inflowing power increases from $\sim 26\%$ during nonstorm periods to $\sim 38\%$ during storm periods, that is, there might be more wave reflection (or additional generation of upward-traveling Alfvén waves) below the satellite during more active times. In the Discussion section, we address this issue further while also comparing these total high-altitude powers to powers recorded below the AAR with regard to Alfvén waves and Alfvénic electrons (i.e., electrons that have been accelerated by Alfvén waves). This

comparison will provide important information on the role of these Alfvén waves.

The development of a storm is synonymous with a large increase (energization) and decay (to prestorm values) of the magnetospheric ring current (13). These two phenomena have been coined the “main phase” and “recovery phase” of storms, respectively. On the ground, they can be identified in magnetometer data from a decrease and rise of the Dst index, respectively (see example below). Additional calculations were performed here to separate the Alfvénic power contributions during storm periods into those occurring during the main and recovery phases (see Materials and Methods). The total integrated hemispherical powers for the main and recovery phases were 10.05 and 6.29 GW, respectively, for downward flow, and 4.07 and 2.62 GW, respectively, for upward flow. The larger values obtained for the main phase are consistent with the established knowledge that the main phase is the more active phase, when solar wind energy input into the magnetosphere is greatly enhanced and the geomagnetic field experiences episodes of extraordinary fluctuations (2). In contrast, the recovery phase presents a phase when the enhanced solar wind energy input stops or is much reduced and the magnetosphere slowly returns to its prestorm state. The recovery phase typically lasts much longer (up to days) than the main phase (up to several hours).

A closer inspection of the global longitudinal and latitudinal developments of Alfvén wave activity reveals the following information. The downward Poynting flux distribution for nonstorm periods (Fig. 2A) shows two distinct regions of enhancement (red, yellow, and lighter blue bins), located on the dayside between 7.5 and 16.5 magnetic local time (MLT) and on the nightside between 21 and 1.5 MLT. The enhanced nightside region is located at around 66° to 74° magnetic latitude, which is more equatorward than the enhanced dayside region at around 75° to 80° magnetic latitude. In contrast, during the storm periods (Fig. 2B), enhanced Poynting flux is present at all longitudes, including the two regions of much reduced Poynting flux on the flanks (near 6 and 18 MLT) apparent in the nonstorm

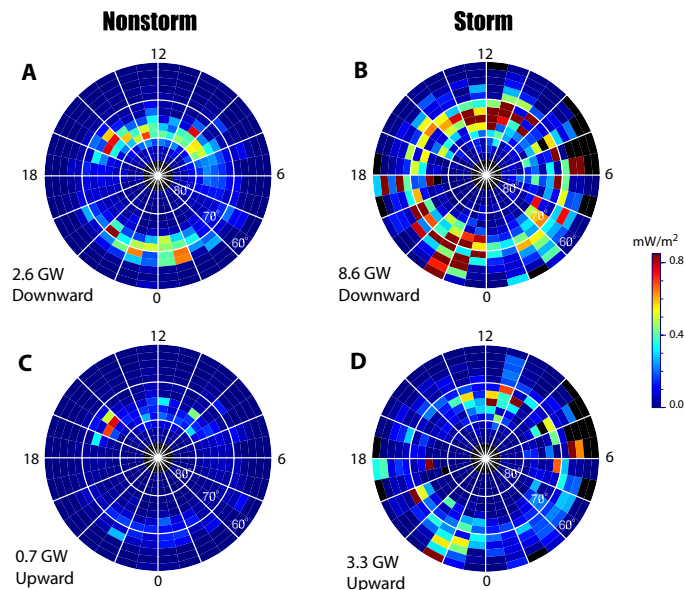


Fig. 2. Morphology of in situ Poynting flux during nonstorm and storm periods. (A) Global distribution of average wave Poynting flux, as a function of magnetic local time (MLT) and latitude, flowing toward Earth (labeled “Downward”). The view is onto the polar-auroral region, with the magnetic north pole in the center. The upper and lower halves correspond to dayside and nightside, respectively. The electric and magnetic field data for calculating Poynting fluxes were measured between 4 and 7 RE (geocentric distance) in the Northern Hemisphere over a period of 6 years (see Fig. 1B for the orbital ellipsoid). The Poynting fluxes shown were scaled along converging magnetic field lines to ionospheric altitudes (100 km) under nonstorm conditions ($-20 \text{ nT} < \text{Dst} < 0 \text{ nT}$). Each bin covers 2° magnetic latitude times 0.75 hour local time. Circles represent magnetic latitudes (60° , 70° , and 80°); radial lines indicate local times (e.g., 6, 12, 18, and 24). The black circle in the center was not analyzed. The number at the lower left corner of each panel is the total hemispherical ($>60^\circ$) power for each distribution. (B) Same as (A) but under storm conditions ($\text{Dst} < -40 \text{ nT}$). For a few bins (black), Polar did not encounter storm conditions; hence, no Poynting flux values are shown. The color scale is the same as in (A) for comparison purposes, which, however, causes some bins to saturate at the highest value. (C and D) Corresponding average Poynting flux distributions flowing toward the magnetosphere (labeled “Upward”).

distribution. Another difference in the storm distribution is the occurrence of enhanced Poynting flux at lower magnetic latitude on the nightside (down to the lowest value, 60° , shown in the figure), while during the nonstorm periods, it does not show below 66° on the nightside. Similarly, on the dayside, intense Poynting flux appears at lower latitudes during storm conditions. There is also an expansion of the region of enhanced Poynting flux toward higher latitudes on the nightside. Together, the upper and lower latitudinal expansions (for all local times) of enhanced Poynting flux form a quasi-oval band, the width of which is increased at nearly all local times during storms. The spatial distributions for nonstorm and storm periods are morphologically similar in many details to the statistical location of the aurora for different degrees of geomagnetic activity [e.g., (15), see also the last paragraph in this section]. Furthermore, the very distinct spatial features of both Poynting flux distributions can also be found in spatial distribution maps of Alfvén waves and Alfvénic electrons, as recorded at altitudes below $\sim 4000 \text{ km}$ (i.e., below the main part of the AAR), during nonstorm and storm periods. In the Discussion section, we will expand on these comparisons and also discuss their ramifications.

The latitudinal broadening of intense Poynting flux, as seen in the global distribution maps in Fig. 2, can also be tracked during individual storms. This is illustrated in Fig. 3, showing the Poynting flux variations (mapped to ionospheric altitude) along Polar’s orbit during a period of 28 days, which includes a moderate storm ($-50 \text{ nT} > \text{Dst} > -100 \text{ nT}$) and a major storm ($-100 \text{ nT} > \text{Dst} > -250 \text{ nT}$). Two magnetospheric models were applied for the magnetic mapping for comparison (see Materials and Methods). The mapping differences between both models vary between 0° and 5° in latitude, with the T01 model typically mapping regions of intense Poynting flux to lower latitudes during more increased geomagnetic activity (i.e., smaller Dst values). However, the general trend toward an expanded Poynting flux band during increased geomagnetic activity is observed with both models, and therefore, we only describe the T01 model results. The satellite’s orbital plane was approximately aligned along 21 to 23 MLT (nightside) and 10 to 11 MLT (dayside) (see inset in Fig. 3B). Every 18 hours (orbital period), the satellite crossed the dayside (Fig. 3A) and nightside (Fig. 3C) polar-auroral regions while encountering a region of enhanced Poynting flux ($>1 \text{ mW/m}^2$; green, yellow, and red colors). Outside of this enhanced band, typical Poynting flux values are orders of magnitude smaller ($<0.1 \text{ mW/m}^2$). The width and location of the enhanced Poynting flux band vary between $\sim 50^\circ$ and $\sim 85^\circ$ magnetic latitude throughout this time interval, in accordance with disturbance levels (Dst) shown in Fig. 3B. For example, from April 20 to April 23, the magnetosphere was in a nonstorm state with a Dst of approximately -10 nT . The upper and lower envelopes of the intense Poynting flux band are located at $\sim 75^\circ$ and $\sim 65^\circ$, respectively, in the nightside (Fig. 3C). This corresponds to the global spatial pattern shown during nonstorm periods (see Fig. 2A; between 21 and 23 MLT). After April 23, the Dst index shows several sharp negative deflections, labeled 2 to 5 alongside vertical lines. Each deflection corresponds to an expansion of the enhanced Poynting flux band to lower magnetic latitude, either on the dayside or nightside (cf. superposed white Dst line in Fig. 3, A and C). The most intense and widest band with the lowest expansion (close to 50°) occurred during the main phase of the major storm (Dst, $\sim -200 \text{ nT}$; line 5), while Polar was on the dayside (Fig. 3A). After this expansion, there is a clear trend on both dayside and nightside for the enhanced band to return to prestorm latitudes until May 16, when Dst reached 0 nT again. However, on the nightside, two Poynting flux enhancements to lower latitudes appeared (May 8 and 11; Fig. 3C), during the storm recovery, that were not accompanied by stronger Dst deflections. It is known that the storm recovery phase continues to experience recurrent nightside substorms (which are further explained below), during which the magnetotail undergoes large-scale magnetic field reconfigurations, which could be responsible for these expansions. In contrast, the dayside magnetosphere is typically unaffected by nightside substorm activity and thus does not show correlated expansions during the storm recovery (Fig. 3A). In addition, it is important to remember that the satellite’s orbit takes about 18 hours for one completion. Thus, depending on where the satellite was along its orbit during a storm intensification (deflection of Dst), the recorded Poynting flux could have occurred on the dayside or nightside. Moreover, the satellite was not in the Northern Hemisphere auroral zone at all times and thus could easily have missed some expansions during times of large deflection of Dst. This orbital dependence can also cause delays and underestimates of the expansion motion as recorded in the enhanced Poynting flux band. With that in mind, it is also interesting to note

that the first expansion toward the lower latitude of the enhanced band, as recorded on the dayside (marked by line 1), coincided with the initial phase of the storm (positive deflection of Dst above 0 nT). The onset of this phase is called the “storm sudden commencement” and corresponds to the first dayside compression of the magnetosphere caused by the shock front of the storm (14). The satellite was on the dayside at this time and thus recorded this compression that caused an expansion to the lower latitude of more intense Poynting flux.

Storms occur far less often than nonstorm periods. Therefore, while the satellite traversed all bins throughout the 6-year period, it spent about 39 days (total) during storm periods in the bins and 247 days (total) during nonstorm periods. This difference in coverage led to more variation among bins in the storm distributions (Fig. 2, B and D). To capture this effect, Fig. 4 shows storm and nonstorm integrated powers (downward) as a function of MLT (see Materials and Methods). For the nonstorm distribution (Fig. 4B), two regions at around 5 and 18 MLT

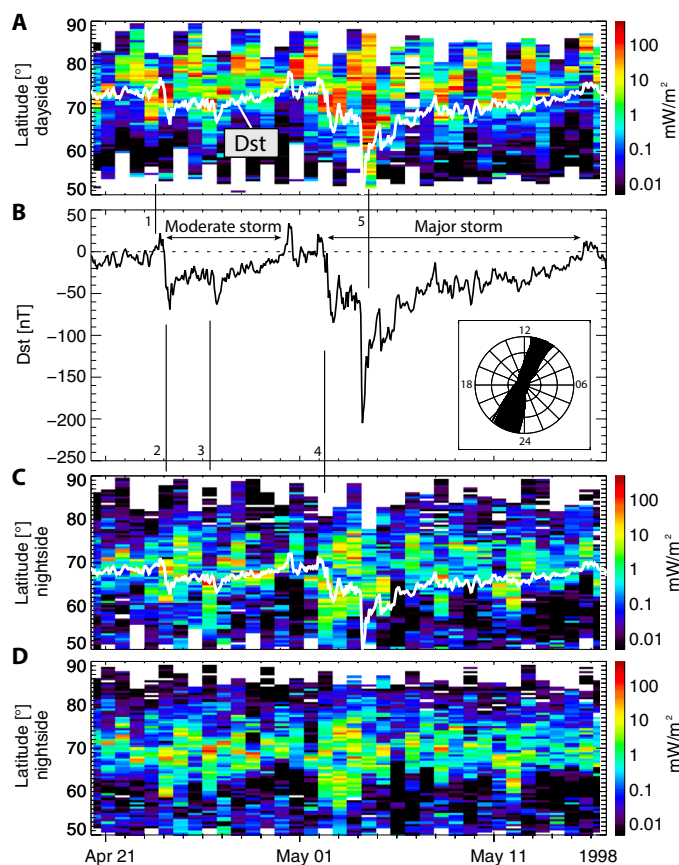


Fig. 3. Tracing Poynting flux along Polar's orbit during a period of 28 days, which includes a moderate storm and a major storm. (A) Peak values of Poynting flux binned by 0.5° magnetic latitude (y axis) versus days (x axis) and mapped using the T01 model. Each column represents the section of a Polar orbit within 50° and 90° magnetic latitude. Only values obtained when Polar was 90° on the dayside are included. The Dst curve [from (B)] is overlaid (white line) with arbitrary scale for illustrative purposes. (B) Dst index versus time, with labels indicating a moderate and a major storm. Numbered vertical lines (1 to 5) refer to the features in the panels above and below (see text). The inset shows Polar's daily orbits during the time period shown here projected onto the latitude-local time plane. (C) Same data quantity as in (A) but for the nightside and with the Dst curve overlaid. (D) Same data quantity as in (A) but for the nightside. However, the mapping was performed using the dipole model for comparison.

show the smallest powers (as is also visible on the flanks in Fig. 2A). In addition, the variations (green-shaded area) are smaller compared with other local times, reaffirming that the flanks consistently show the smallest activity on average during nonstorm times. The storm distribution (Fig. 4A) exhibits larger variations while also confirming that the regions around 5 and 18 MLT show significant activity as well.

Last, Fig. 5 shows the peak values of Poynting flux recorded in each bin (for the entire study period) during storm periods (see Materials and Methods) to assess the capability of the Alfvén waves to provide sufficient energy flux to drive auroral processes. While this has been verified in many case studies (see Discussion), here we confirm it for storm conditions for a larger dataset. The dashed curves outline the statistical auroral oval for geomagnetically active periods (15). Most values inside this statistical oval are larger than 5 mW/m^2 , with many values greater than 100 mW/m^2 (even up to 500 mW/m^2). It is noted that an energy flux of 1 mW/m^2 would be sufficient to cause conjugate, visible auroras (16). It is also noted that the premidnight-to-midnight region shows the largest collection of intense Poynting fluxes. This region coincides with the location of the so-called substorm aurora (17). While substorms per se are not the focus of this study, the reader is here briefly informed about their significance. In addition to a storm, a substorm is another major magnetospheric dissipation mechanism in the solar wind–magnetosphere–ionosphere system, causing a global re-configuration of the magnetosphere (2). While storms encompass the entire magnetosphere, substorms (mostly) only affect the nightside magnetosphere. This also means that substorms exhibit much smaller overall energy flow/dissipation within the magnetosphere during a much shorter duration (one to a few hours versus many hours to several days for storms) (18). There are many detailed differences, some of which are still debated, and to discuss them here is outside the scope of this report [see (19) for a discussion]. Substorms occur during storms as well; they typically occur at an increased rate, and the associated aurora is more intense than for substorms that occur during nonstorm periods (20). Since it has been reported that energetic Alfvén waves are characteristic for substorms, especially during the expansion phase (21), the grouping of intense Poynting flux bins

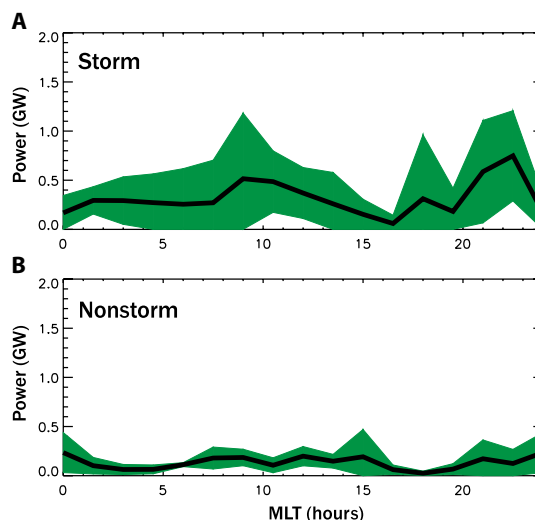


Fig. 4. Alfvén wave power along MLT. (A) Storm condition ($\text{Dst} < -40 \text{ nT}$). (B) Nonstorm condition ($-20 \text{ nT} < \text{Dst} < 0 \text{ nT}$). In both panels, the solid line shows mean values, and the green-shaded area shows 1 SD away from the mean.

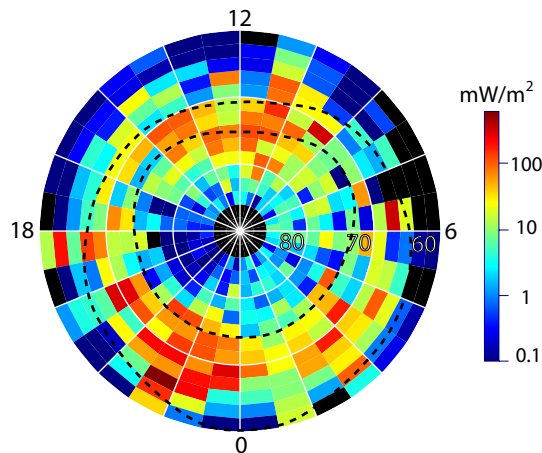


Fig. 5. Morphology of in situ peak Poynting flux during storm periods.

The global distribution of peak wave Poynting flux during storms ($Dst < -40$ nT) flowing toward Earth as measured at high altitude (4 to 7 RE geocentric) in the Northern Hemisphere obtained from 6 years of Polar measurements and scaled along converging magnetic field lines to ionospheric altitudes (100 km). Each bin covers 2° magnetic latitude times 0.75 hour local time. Circles represent magnetic latitudes (60° , 70° , and 80°); radial lines indicate local times (e.g., 6, 12, 18, and 24). The black circle in the center was not analyzed. For a few bins (black), Polar did not encounter storm conditions; hence, no Poynting flux values are shown. The two dashed oval-shaped curves delineate the statistical auroral oval for geomagnetically active periods (15).

in the premidnight-to-midnight region could be a reflection of this fact, although we caution that it requires further investigation.

DISCUSSION

Using the unique location of the Polar satellite, our results provide the first global energy budget calculation for Alfvén waves above the AAR in relation to storm phases. The inflowing energy rate (power) over the entire polar-auroral region during general storm conditions was 8.6 GW, while a separation into the main phase and recovery phase yielded 10.05 and 6.29 GW, respectively, in comparison to 2.59 GW during nonstorm periods. This corresponds, for example, to a 3.9-fold increase during the dynamic main phase, compared to nonstorm periods. Peak Poynting flux values for individual storm Alfvén wave events were found to be up to 0.5 W/m^2 . While the outflowing power was much less, the proportion of outflowing power in relation to the inflowing power increased during more active periods. For example, during nonstorm periods, it was $\sim 26\%$, and during storm periods, it was $\sim 38\%$. It is informative to compare our values with power estimates for auroral luminosity (0.1 to 1 GW), auroral precipitation (1 to 10 GW), and ionospheric Joule heating (10 to 100 GW) during substorms (18). Placed in this context, our results demonstrate the relative importance of Alfvén waves as an intermediate energy carrier during storms, that is, times of enhanced energy transport demands between the magnetosphere and the ionosphere.

We also assessed the global spatial distribution of Alfvén wave power in the polar-auroral region above the AAR. During nonstorm periods, the dayside cusp and the midnight region were the preferred regions of intense Alfvén wave power. In contrast, during storms, Alfvén wave power was enhanced at all local times, including the dawn and dusk flanks, and it appeared over a significantly broadened

latitudinal band (as low as 50°). It is emphasized that these distributions are based on values averaged over 6 years of data. Thus, individual nonstorm and storm events could certainly deviate at times. The widening of the band of enhanced Alfvén wave activity was also demonstrated for two successive storms. A trend was noted that the more intense the storm (lower Dst value), the lower the latitudinal occurrence of intense Poynting flux. This spatial expansion can be compared with phenomena at magnetically conjugate, remote regions, on both the dayside and nightside, to shed light on possible wave source regions (see Fig. 1C as reference). On the dayside, storms cause further compression of the magnetosphere and enhanced magnetic flux erosion (2, 22). This inward motion corresponds to a motion toward lower latitude in the conjugate high-latitude cusp region. Synonymously, storms are accompanied and, in fact, caused by prolonged periods of negative interplanetary magnetic field (IMF), leading to enhanced reconnection and increased energy transfer into the dayside magnetosphere (23). Alfvén wave activity is also increased during periods of negative IMF in the equatorial magnetosheath region, which connects to the high-latitude cusp (10), and reconnection has been shown to launch Alfvén waves in the dayside magnetopause (24). On the nightside, enhanced broadband low-frequency electromagnetic wave activity was recorded at lower L shells (corresponding to lower magnetic latitudes in the polar region) during storm periods while also azimuthally spreading over the entire nightside (11). While the here-reported changes in the spatial distribution of Alfvén wave activity directly above the AAR from nonstorm to storm periods are consistent with changes of wave activity at these remote magnetospheric regions, it remains to be shown in future works whether these are causal relationships.

A comparison of our results with low-altitude estimates of energy budgets provides evidence for enhanced dissipation/deposition of Alfvén waves inside the AAR during storms. Hatch *et al.* (25) investigated the global spatial distributions of Alfvén wave power and Alfvénic electron energy flux during nonstorm and storm periods using the Fast Auroral Snapshot Explorer (FAST) satellite at altitudes below ~ 4000 km. This altitude range covers the lower end of the AAR and below, and thus, it is a region that should see some of the effects of higher-altitude Alfvén waves. Their global spatial distributions [Figs. 2A and B of (25)] of Alfvén waves and Alfvénic electrons during nonstorm and storm periods are morphologically remarkably similar to the here-reported Poynting flux distributions above the AAR during similar geomagnetic conditions. While this morphological similarity suggests causal connections, with the high-altitude Alfvén waves being the driver of the low-altitude signatures, it assumes an energy transfer scenario inside the AAR that has been reviewed by (12), even though some details are still awaiting observational confirmation. In brief, the mostly nondissipative, large-scale MHD Alfvén waves transfer their energy into the dissipative, smaller-scale kinetic Alfvén wave (KAW) inside the AAR (also called inertial Alfvén waves in the lower-altitude range) followed by electron acceleration via the magnetic field-aligned electric field of the KAW. There is observational evidence for this sequence of events from conjunction studies, which are high-altitude observations combined with low-altitude observations on the same (or very close) flux tube (26, 27). Both studies showed that the energy flux of electrons increases from high to low altitudes inside the AAR, and at the same time, the energy flux of large-scale Alfvén waves decreases, while small-scale Alfvén waves are generated.

From their global distributions, Hatch *et al.* (25) calculated, in a similar fashion as was done here, the total integrated energy rates recorded below the AAR for nonstorm periods, storm main phase, and storm recovery phase. For comparison, we reproduced the FAST-based values together with our results in Table 1. First, it is noted that there is significantly more power (in the form of Alfvén waves) entering the AAR during all three phases than those observed below the AAR in the Alfvén waves and the electrons (taken separately). Second, if we subtract the power of outflowing Alfvén waves from the Alfvén wave power entering the AAR at Polar's location, then the "net" power inflow into the AAR is still larger than the low-altitude electron energy flux and the low-altitude Alfvén waves during the nonstorm period and main phase, but not during the recovery phase. Third, if we combine both contributions (electrons and Alfvén waves) from the FAST data, then the resulting net deposition is only exceeded by high-altitude "net" power inflow of Alfvén waves during the nonstorm phase, but not during the main and recovery phases. However, there are also two caveats that make such a comparison somewhat uncertain. We used quotation marks for the "net" power of Alfvén waves at Polar because it is not known for certain that there are no upward-traveling Alfvén waves that were generated below the satellite (e.g., in the ionosphere; see more details below), in which case the quoted value for "net" inflow in Table 1 would increase. Furthermore, it is noted that Hatch *et al.* (25) did not specify the flow direction of the low-altitude Alfvén waves, which leaves it open to whether the waves traveled exclusively downward or existed as a mixture of downward- and upward-traveling waves. This would affect the energy balance as well. Nevertheless, we can still summarize that there is significantly more Alfvén wave power entering the AAR from above than there is power associated with either of the low-altitude phenomena, and the majority of the Alfvén wave power is deposited below the satellite. However, since it appears (when ignoring the two caveats but also in light of the discussion in the next paragraph) that the high-altitude Alfvénic power might not be large enough to drive both low-altitude phenomena during the storm phases, future work

should also include additional contributions in the energy budget, as discussed next.

In the analysis of the energy budget, several additional contributions need to be considered. Alfvén waves can also contribute to Joule heating in the ionosphere. While we have no estimate from our analysis, others have suggested using event case studies that the Alfvénic contribution to Joule heating in the auroral zone should be less than 30% of the total Alfvén wave power entering the AAR (26). It is noted that Pc5 field line resonances (standing Alfvén waves) can contribute a significant amount of Joule heating over large spatial regions (28). However, we have not included Pc5 field line resonances in our analysis because they lie outside our frequency band (see Materials and Methods). In addition to electron acceleration, it has been suggested that ions can be accelerated by Alfvén waves, contributing to ion outflow into the magnetosphere (29). Global energy rate estimates of this contribution do not exist, but it has been pointed out that on the nightside, the energy flux of upward-traveling ions is much smaller than that for precipitating electrons (7). Applied to our study, these two additional contributions would drain the available power of the high-altitude Alfvén waves reported here. On the other hand, there are additional energy sources of relevance that can contribute toward the auroral processes discussed here. First, simultaneously occurring smaller-scale KAWs at Polar's altitude also carry energy into the AAR but were not included in our analysis (as outlined in Materials and Methods). However, by one estimate, their power is less than 25% of the MHD Alfvén wave power while also showing a more bidirectional flow, implying less net flow toward the ionosphere (30). Second, field-aligned moving electrons have been shown to exist above the AAR, exhibiting features of Alfvénic acceleration. An estimate of their total energy flux does not exist either. Third, the ionosphere plays an important—and not only passive—role in the coupled magnetosphere-ionosphere (M-I) system. For example, it has been reported that during storms, Alfvén waves are also generated in the ionosphere, followed by outward propagation toward the magnetotail (31), which could potentially add to the upward flow of Alfvén waves observed in the Polar data, and thus should be included in the overall energy balance. While these additional contributions complicate the total energy balance significantly, it can still be concluded that the MHD Alfvén waves are essential contributors to the M-I coupling during storms. Moreover, these additional considerations imply that similar large-scale Alfvén waves dissipate above the Polar's altitude, which has been shown by (8). Thus, our estimates of MHD Alfvén wave power at the top edge of the AAR should be a lower estimate of the actual total power of MHD Alfvén waves generated along the entire auroral current circuit.

Last, we relate the high-altitude Alfvén wave observations to the global aurora. It is now well established that Alfvén waves carry sufficient energy flux from the outer magnetosphere to the auroral region and provide a mechanism for auroral acceleration processes, causing visible aurora [see reviews by (12) and (9)]. In the case of storm Alfvén waves, as reported here, the mapped peak Poynting flux values (up to 500 mW/m²) are by far large enough to potentially cause visible conjugate aurora, the lower threshold of energy flux being 1 mW/m² (16). However, we caution that we did not show this coupling for individual events during different phases of storms. Instead, the emphasis in this study was on multiyear average statistics, which provide some evidence for a global participation of Alfvén waves in the storm aurora. First, we discussed the remarkable

Table 1. Comparison of global powers for the Northern Polar Region.

Satellite	Nonstorm	Main phase	Recovery phase
Polar (above AAR)*			
Alfvén wave _{down} (GW)	2.59	10.05	6.29
Alfvén wave _{up} (GW)	0.67	4.07	2.62
Net deposition (GW) [†]	1.92	5.98	3.67
FAST (below AAR)[‡]			
Alfvén wave (GW)	0.54	2.62	1.75
Electron precipitation (GW)	0.91	5.08	4.27
Net deposition (GW) [§]	1.45	7.70	6.02

*Polar study period: January 1997 to December 2002. †Net deposition at Polar is not necessarily the true deposition below the AAR (see text for explanation). ‡FAST study period: October 1996 to November 1999 [from (25)]. §Calculated under the assumption that all Alfvén wave power at FAST flows toward the ionosphere (i.e., no upflowing Alfvénic power).

similarity of global morphological features in the high-altitude Poynting flux distribution (reported here) compared to low-altitude observations of precipitating Alfvénic electrons, with the latter being presumably powered by the former along auroral field lines. Consequently, as seen in Table 1, the precipitating electron power dominates over the residual Alfvénic power during all storm phases. It is assumed that these precipitating electrons generate auroras. Second, a comparison with the statistical location of auroras for different degrees of geomagnetic activity is instructive (15). We refer the reader to Fig. 5 of (15) for comparison. The shape and latitudinal width of the first auroral band from the left (less active periods) and of the farthest right auroral band (most active periods) are very similar to the here-reported enhanced Poynting flux distributions during non-storm and storm periods (Fig. 2), respectively (see also Fig. 5). Therefore, the reported Alfvén wave power is a candidate driver for some global auroral enhancements during storms. In addition to these statistical auroral patterns, storm auroras can also encompass the entire auroral oval instantaneously. As an example of a storm aurora, Fig. 1A shows the auroral development during a storm. In these images, it can be seen how rapidly the aurora developed, forming a largely increased luminous oval around the magnetic pole within 10 min. These active periods should correspond to impulsive reconfiguration of the magnetic field, which are especially prone to Alfvén wave generation (32). While it appears very reasonable to conclude that the global broadening of intense Alfvénic Poynting flux is related to some parts of the globally broadening storm aurora, we emphasize that we do not argue here that the entire storm aurora is driven by Alfvén waves. In the literature, the aurora has been attributed to at least three types, which are called quasi-static aurora, Alfvénic aurora, and diffuse aurora (among other names). The auroral belts shown in (15) include all types of aurora. It has been a challenge to determine the global contributions of each type to the aurora. Under various geomagnetic conditions (but not storms per se), estimates of Alfvénic aurora range between 6 and 50% of the total aurora (33–35), with the lower estimate believed to be too low (36). To what extent the storm aurora is Alfvénic is not known as of yet, and its determination, is outside the scope of this study.

MATERIALS AND METHODS

Global distributions

The global Poynting flux distributions (Fig. 2) were generated from a multiyear database containing data from the Polar satellite. The Polar satellite had an 18-hour elliptical, polar orbit with perigee and apogee of 1.8 and 9 RE, respectively, measured from the center of Earth. During the course of 1 year, its orbital plane precessed by 360°, thus covering the entire Northern Hemisphere throughout the year with equal coverage of each MLT (Fig. 1C) and avoiding biasing toward certain MLT regions. For this study, we incorporated 6 years of data (1997–2002), from the solar minimum to the solar maximum of solar cycle 23 (Fig. 1A). The measured data were electric (\mathbf{E}) and magnetic (\mathbf{B}) field data collected in the range from 4 to 7 RE (geocentric distance) in the Northern Hemisphere (so as to be above the nominal AAR), which were then used to calculate the Poynting flux for the entire database: $\mathbf{S} = \delta\mathbf{E} \times \delta\mathbf{B}/\mu_0$. $\delta\mathbf{E}$ and $\delta\mathbf{B}$ are the perturbation fields in the band from 6 to 180 s in the spacecraft frame. The perturbation fields were obtained from the full three-dimensional magnetic field vector and two vector components of

the electric field [see (33) for a discussion on the validity of leaving out the satellite's spin-axis component of the electric field]. It is noted that the methodology in (33) is identical to the one applied here, with one exception, namely, these authors additionally averaged the Poynting flux over 30-s intervals to reduce power of standing waves (which were observed in this range). Later, it was also reported that higher-frequency Alfvén waves (i.e., smaller periods) show more reflective behavior inside the AAR (26, 37). As a result, our modified analysis method produces somewhat more outflowing Poynting flux compared with (33).

To obtain the component of the wave Poynting flux that flows along the background magnetic field, the Poynting flux, \mathbf{S} , was projected onto the background magnetic field, \mathbf{B} : $S_p = \mathbf{S} \cdot \mathbf{B}/|\mathbf{B}|$. All Poynting flux values were scaled along converging magnetic field lines to ionospheric altitudes (100 km) under the assumption of dissipation-free propagation: $S_I = S_H \cdot B_I/B_H$, where the indices I and H indicate the ionospheric and high-altitude values, respectively. For the ionospheric field strength, a fixed value of 50,000 nT was applied. This mapping method allows comparisons with other studies that project energy fluxes (both waves and particles) onto the ionosphere and has been described in more detail by (38). The Poynting flux database was then binned according to magnetic latitude and MLT ($2^\circ \times 0.75$ hour per bin) for the Northern Hemisphere.

The binned data were further sorted according to the Dst values (storm: $\text{Dst} < -40$ nT; nonstorm: -20 nT $< \text{Dst} < 0$ nT) and according to flow directions as recorded at Polar's location (toward the AAR and away from the AAR). For all distributions (Fig. 2, A to D), the color scale was chosen to be the same for comparison purposes, causing the highest values in the storm distributions to saturate at the highest value (brown). Actual peak values are given in Fig. 5 (see below).

For the calculation of total hemispheric powers ($>60^\circ$ magnetic latitude) in Fig. 2, all averaged and projected Poynting flux values (per bin) were multiplied by the respective area at 100 km and summed. Downward (positive Poynting flux) and upward (negative Poynting flux) total powers were calculated separately while accounting for the total time spent in each bin. Noise levels of <0.1 mW/m² (corresponding to the dark blue in the maps) were removed in this calculation, slightly reducing the total power. While not shown in Fig. 2, storm events were also separated according to storm main phase and storm recovery phase, and then total hemispheric powers were similarly calculated (see Table 1). In addition to the general storm condition ($\text{Dst} < -40$ nT), for the main phase, a negative slope in Dst was required, while a positive slope in Dst was needed for the recovery phase.

Mapping of magnetic field

For the mapping from Polar's location to ionospheric altitudes, we applied two models (see Fig. 3): (i) the dipole model and (ii) the Tsyganenko 2001 model (T01) (39, 40). While the dipole model is fixed, the T01 model allows for a variable global magnetic field of the inner and near magnetosphere, including the effects of the ring current, for different interplanetary conditions and ground disturbance levels. Thus, it requires the solar wind ram pressure, Dst, and the transverse components of the IMF as input parameters. Because of these additional requirements, we limited its application to event cases, of which Fig. 3 shows one case. Geomagnetic mapping is notoriously difficult (or even impossible) during geomagnetic disturbed periods in M-I coupling; however, for confirming the expansion of the global, spatial distributions (shown in Fig. 2), the dipole model suffices.

Power versus MLT distribution

The data points (mean values and SDs) were calculated by first separating the entire database into individual years (1997 to 2002). Then, for each year, the averaged spatial distributions (similar to Fig. 2) were generated. For each yearly distribution, integrated (over all latitudes) powers were calculated with respect to MLT sectors. Hence, for each MLT sector, six values were available (one for each year), which were used to calculate the means and SDs plotted in Fig. 4.

Peak distributions

During a storm, which can last for more than 1 day, auroral and magnetospheric activity fluctuates. Similarly, it is not expected that Alfvén wave activity is at its highest level throughout the entire storm period. Thus, the average Poynting flux distributions shown in Fig. 2 contain a combination of different intensities. To capture the possible maximum Poynting fluxes (downward) throughout the entire AAR oval, the database of each bin was searched for the maximum value during storm conditions ($Dst < -40$ nT). These maximum values are plotted in Fig. 5 (in the same format as Fig. 2), revealing peak values of well over 100 mW/m^2 in some parts of the oval (see further discussion in the main text).

Assumptions and limitations

Here, we address two fundamental aspects of the applied method, namely, the assumptions made and the limitations resulting from these assumptions. Our main assumption is that the spectrum with periods in the range of 6 to 180 s (or, alternatively, 6 to 167 mHz) largely contains shear Alfvén waves, which is based on observational, numerical, and theoretical considerations. Numerous observational event case studies have identified shear Alfvén waves in this band, with wave velocities being similar to the local Alfvén speed, as expected from MHD calculations [(7, 21, 41–43) to list a few, but also see the review by (9) for a more extensive list]. While the most energetic Alfvén waves have been shown to occur during substorms and storms (7, 26), their presence—albeit with much reduced amplitude—has also been shown during geomagnetic quiet periods (38). In detailed numerical studies, Streltsov *et al.* (44) and Streltsov and Lotko (45) showed that the large-amplitude Alfvén wave events in the Polar database can be ascribed to MHD Alfvén waves generated in the magnetotail. Comparisons of large-database statistical studies are also instructive. For example, the global spatial distribution of Alfvén waves (same wave band as used here) above the AAR revealed their global participation in the M-I coupling (33). Very similar global spatial distributions of Alfvén waves and Alfvén-accelerated electrons were reported from low-altitude satellites below the AAR (34, 46–49), which again argues that the chosen wave band captures well the Alfvénic regime. Furthermore, global MHD simulations (50) reproduced to a remarkable degree both the observed spatial distribution and also the intensity of Alfvénic power flowing from the magnetotail to the same altitudes as those reported by (33). Furthermore, theoretical considerations corroborate these findings by showing that the chosen band should be dominated by MHD inductive M-I coupling (i.e., Alfvénic coupling), as opposed to the electrostatic M-I coupling, such as quasi-static currents (51).

From these studies, it is argued that the chosen wave band mostly captures the large-scale, nondispersive MHD regime of Alfvén waves. It is cautioned that because of the ambiguity of temporal and spatial effects due to the relative motion of the spacecraft and plasma carrying the waves, it is not possible to obtain the actual perpendicular

scales of the large-scale Alfvén waves. This issue is discussed in (7) as it applies to Polar satellite observations. It also implies that the period/frequency band chosen for our study refers to the spacecraft frame, so that the period/frequency can be Doppler shifted from the values in the plasma frame. In the Discussion section, we compared the Polar observations with global distributions of Poynting flux determined from the FAST satellite, which orbits at a much lower altitude (<4000 km). While it was attempted to determine the spatial transverse scale, from which the inertial regime of the low-altitude Alfvén waves was estimated (25), the ambiguity in wave period/frequency of the FAST waves remained. However, the justification for this comparison has been discussed by others [e.g., (12, 49, 52)]. One of the main arguments provided is that KAWs are strongly damped (highly dissipative), preventing them from traveling far. Hence, Chaston (12) wrote, “the most obvious local energy source for these waves may be the large-scale nondispersive, nondissipative Alfvén waves commonly observed as part of the Alfvén wave spectra.” Furthermore, the conversion from large scales to small scales along auroral field lines has been modeled for low-frequency waves [e.g., (53) and references therein].

Here, we extended the database from that used in (33) to contain 6 years of data while applying the same methodology for pre-processing, followed by the additional storm/nonstorm separation. It is thus reasonable to assume that our results again capture most of the MHD Alfvén wave physics in this specific wave band for the extended period. Nonetheless, it is unproven (and unlikely) that all recorded field perturbations are Alfvénic. For example, near the subsolar (dayside) magnetopause, slow mode waves have been observed in this wave band [e.g., (54)]; hence, it cannot be ruled out that those waves are included in our statistical database as well. However, their Poynting flux ($\sim 1 \text{ mW/m}^2$ mapped to the ionosphere) is at least an order of magnitude smaller than the Poynting flux of the energetic Alfvén waves observed above the AAR by Polar (~ 10 to 100 mW/m^2 mapped to the ionosphere). Thus, the slow mode waves do not contribute significantly to the overall Poynting flux distributions presented here. Furthermore, quasi-static FACs also supply Poynting flux to the AAR and the ionosphere, such as the large-scale region 1 and 2 currents and the substorm current wedge [see reviews by (6, 55)]. On both the dayside and nightside, studies have shown that our chosen filter band effectively removes the large-scale DC component of electric and magnetic fields (30, 54). Schriver *et al.* (42) reported a comparison of FAST and Polar conjunctions, which illustrated the spatial differences between Alfvén waves and large-scale FACs both below and above the AAR. Associated with each large-scale current is also its temporal evolution. For example, Maynard *et al.* (41) applied a low-pass filter to field data recorded near the inner edge of the plasma sheet, resulting in mostly downward Alfvénic Poynting flux into the ionosphere with periods in the Pi2 range (40 to 150 s). In their study, it was argued that this Alfvénic Poynting flux is involved in establishing the field-aligned current of the substorm current wedge. Because this period range is included in our chosen band (6 to 180 s), our method captures those temporal aspects of large-scale FACs.

In contrast, it is more likely that quasi-static small-scale FACs, which could be embedded in larger-scale FACs, can appear to be waves in the spacecraft measurements because of the perpendicular motion between the current structure and spacecraft. To separate the Alfvén waves from quasi-static small-scale currents, two common approaches have been used in the literature. For example, Johansson

et al. (56) identified both Alfvén waves and quasi-static currents in the same altitude range investigated here using the Cluster mission, which comprises four satellites flying in a constellation. However, the static currents reported had smaller Poynting fluxes (nearly one order of magnitude compared to those of reported energetic Alfvén waves). Nonetheless, it cannot be ruled out that larger Poynting fluxes associated with the quasi-static small-scale structures also exist at Polar's location. However, this multisatellite analysis is not applicable to our database (using the single Polar satellite), and it would also be unrealistic given the size of our database. Another method is to relate the so-called E-to-B ratio to the local Alfvén speed, which would confirm an Alfvénic nature if both values were identical. However, this approach also carries its caveats and suffers from large uncertainties when not looked at carefully case by case. For example, the plasma density is necessary to determine the local Alfvén speed but is difficult to obtain and usually carries large uncertainty. Ideally, information about the ion species and their relative proportions is required, as these factors affect the density and, in turn, the local Alfvén speed. Furthermore, the interaction of Alfvén waves of various temporal and spatial scales with the ionosphere and regions of parallel electric fields, such as the AAR below Polar's location, can lead to more complicated phase relationships between δE and δB , affecting the E-to-B ratios in unpredictable ways (57, 58, 45). These uncertainties and constraints led authors of earlier studies to allow for variations in the E-to-B ratio of up to an order of magnitude [e.g., (46, 49)]. These errors would outweigh our assumptions, and therefore, we did not incorporate this additional test.

While there is ample evidence for Alfvén waves in the 6- to 180-s band, as described above, Alfvén waves also occur below and above this band. We have excluded these waves for the following reasons. By also using Polar data in the same altitude range, waves with periods (in spacecraft frame) of less than 6 s were identified as KAWs (30). It was also shown that KAWs occur at much larger distances (18 RE), and since KAWs are highly dissipative due to their magnetic field-aligned electric field component, much of their energy was already transferred onto the surrounding plasma before reaching Polar at 5 RE (8). In a larger study, it was reported that KAWs are launched by fast plasma flows along the magnetotail (59). Hence, to assess the total impact of these smaller-scale waves on the entire magnetosphere, it would be necessary to make observations directly at the source region, which was not done in our study. Instead, we only assessed the MHD component of shear Alfvén waves, which is largely aligned with the background magnetic field. Our method also excludes the bulk of Alfvénic Pc5 field line resonances (periods of 150 to 600 s), which are standing Alfvén waves with Poynting fluxes of alternating directions. Although it was shown that they can have a small net flow direction, which can lead to substantial Joule heating over a large area in the ionosphere (28), it would be difficult (or impossible) to identify their net fluxes in our statistical database without case-by-case verification. Moreover, the Pc5 period range overlaps with the spatial scale of large-scale FACs at Polar's location, making an unambiguous distinction at Polar's location impossible using our statistical method. Despite leaving out the lowest and highest frequencies, it can still be asserted that our chosen band captures the key portion of the Alfvén wave spectrum flowing into the AAR, as evidenced by (i) comparisons with results from low-altitude satellites (see Discussion), (ii) results that relate this band with powering the aurora (33), and (iii) confirmation that the band contains the largest Alfvén waves above the AAR (7, 26).

REFERENCES AND NOTES

- M. Hapgood, Astrophysics: Prepare for the coming space weather storm. *Nature* **484**, 311–313 (2012).
- W. D. Gonzalez, J. A. Joselyn, Y. Kamide, H. W. Kroehl, G. Rostoker, B. T. Tsurutani, V. M. Vasylunas, What is a geomagnetic storm? *J. Geophys. Res.* **99**, 5771–5792 (1994).
- S. J. Perry, Aurora borealis and magnetic storms. *Nature* **22**, 361 (1880).
- J. L. Burch, The fury of space storms. *Sci. Am.* **284**, 86–94 (2001).
- J. Kuijpers, H. U. Frey, L. Fletcher, Electric currents in astrophysics. *Space Sci. Rev.* **188**, 3–57 (2015).
- T. Karlsson, The Acceleration Region of Stable Auroral Arcs, in *Auroral Phenomenology and Magnetospheric Processes: Earth And Other Planets*, A. Keiling, E. Donovan, F. Bagenal, T. Karlsson, Eds. (American Geophysical Union, 2012), vol. 197, pp. 227–239.
- J. R. Wygant, A. Keiling, C. A. Cattell, M. Johnson, R. L. Lysak, M. Temerin, F. S. Mozer, C. A. Kletzing, J. D. Scudder, W. Peterson, C. T. Russell, G. Parks, G. Germany, J. Spann, Polar spacecraft-based comparisons of intense electric fields and Poynting flux near and within the plasma sheet-tail lobe boundary to UVI images: An energy source for the aurora. *J. Geophys. Res.* **105**, 18675–18692 (2000).
- V. Angelopoulos, J. A. Chapman, F. S. Mozer, J. D. Scudder, C. T. Russell, K. Tsuruda, T. Mukai, T. J. Hughes, K. Yumoto, Plasma sheet electromagnetic power generation and its dissipation along auroral field lines. *J. Geophys. Res.* **107**, SMP 14-1–SMP 14-20 (2002).
- A. Keiling, Alfvén waves and their roles in the dynamics of the Earth's magnetotail: A review. *Space Sci. Rev.* **142**, 73–156 (2009).
- Y. Yao, C. C. Chaston, K.-H. Glassmeier, V. Angelopoulos, Electromagnetic waves on ion gyro-radii scales across the magnetopause. *Geophys. Res. Lett.* **38**, L09102 (2011).
- C. C. Chaston, J. W. Bonnell, C. A. Kletzing, G. B. Hospodarsky, J. R. Wygant, C. W. Smith, Broadband low-frequency electromagnetic waves in the inner magnetosphere. *J. Geophys. Res. Space Physics* **120**, 8603–8615 (2015).
- C. C. Chaston, ULF waves and auroral electrons, in *Magnetospheric ULF Waves: Synthesis and New Directions*, K. Takahashi, P. J. Chi, R. E. Denton, R. L. Lysak, Eds. (American Geophysical Union, 2006), vol. 169, pp. 239–257.
- M. Sugiura, Hourly values of equatorial Dst for the IGY, in *Annual International Geophysical Year* (Pergamon, New York, 1964), vol. 35, pp. 9.
- T. Araki, A physical model of the geomagnetic sudden commencement, in *Solar Wind Sources of Magnetospheric Ultra-Low-Frequency Waves*, M. J. Engebretson, K. Takahashi, M. Scholer, Eds. (American Geophysical Union, 1994), vol. 81, pp. 183–200.
- Y. I. Feldstein, G. V. Starkov, Dynamics of auroral belt and polar geomagnetic disturbances. *Planet. Space Sci.* **15**, 209–229 (1967).
- H. C. Stenbaek-Nielsen, T. J. Hallinan, D. L. Osborne, J. Kimball, C. Chaston, J. McFadden, G. Delory, M. Temerin, C. W. Carlson, Aircraft observations conjugate to FAST: Auroral arc thicknesses. *Geophys. Res. Lett.* **25**, 2073–2076 (1998).
- S.-I. Akasofu, The development of the auroral substorm. *Planet. Space Sci.* **12**, 273–282 (1964).
- D. N. Baker, T. I. Pulkkinen, M. Hesse, R. L. McPherron, A quantitative assessment of energy storage and release in the Earth's magnetotail. *J. Geophys. Res.* **102**, 7159–7168 (1997).
- G. Siscoe, Magnetospheric physics-Big storms make little storms. *Nature* **390**, 448–449 (1997).
- R. A. Hoffman, J. W. Gjerloev, L. A. Frank, J. W. Sigwarth, Are there optical differences between storm-time substorms and isolated substorms? *Ann. Geophys.* **28**, 1183–1198 (2010).
- A. Keiling, J. R. Wygant, C. Cattell, M. Temerin, F. S. Mozer, C. A. Kletzing, J. D. Scudder, C. T. Russell, W. Lotko, A. V. Streltsov, Large Alfvén wave power in the plasma sheet boundary layer during the expansion phase of substorms. *Geophys. Res. Lett.* **27**, 3169–3172 (2000).
- M. Wiltberger, R. E. Lopez, J. G. Lyon, Magnetopause erosion: A global view from MHD simulation. *J. Geophys. Res.* **108**, 1235 (2003).
- B. T. Tsurutani, W. D. Gonzalez, The interplanetary causes of magnetic storm, in *Magnetic Storms*, B. T. Tsurutani, W. D. Gonzalez, Y. Kamide, J. K. Arballo, Eds. (American Geophysical Union, 1997), vol. 98, p. 77.
- C. C. Chaston, T. D. Phan, J. W. Bonnell, F. S. Mozer, M. Acuña, M. L. Goldstein, A. Balogh, M. Andre, H. Reme, A. Fazakerley, Drift-kinetic Alfvén waves observed near a reconnection X line in the Earth's magnetopause. *Phys. Rev. Lett.* **95**, 065002 (2005).
- S. M. Hatch, J. LaBelle, C. C. Chaston, Storm phase-partitioned rates and budgets of global Alfvénic energy deposition, electron precipitation, and ion outflow. *J. Atmos. Sol. Terr. Phys.* **167**, 1–12 (2018).
- J. Dombeck, C. Cattell, J. R. Wygant, A. Keiling, J. Scudder, Alfvén waves and Poynting flux observed simultaneously by Polar and FAST in the plasma sheet boundary layer. *J. Geophys. Res.* **110**, A12S90 (2005).
- C. C. Chaston, L. M. Peticolas, C. W. Carlson, J. P. McFadden, F. Mozer, M. Wilber, G. K. Parks, A. Hull, R. E. Ergun, R. J. Strangeway, M. Andre, Y. Khotyaintsev, M. L. Goldstein, M. Acuña, E. J. Lund, H. Reme, I. Dandouras, A. N. Fazakerley, A. Balogh, Energy deposition by Alfvén waves into the dayside auroral oval: Cluster and FAST observations. *J. Geophys. Res.* **110**, A02211 (2005).

28. I. J. Rae, C. E. J. Watt, F. R. Fenrich, I. R. Mann, L. G. Ozeke, A. Kale, Energy deposition in the ionosphere through a global field line resonance. *Ann. Geophys.* **25**, 2529–2539 (2007).
29. C. C. Chaston, J. B. Bonnell, C. W. Carlson, J. P. McFadden, R. E. Ergun, R. J. Strangeway, E. J. Lund, Auroral ion acceleration in dispersive Alfvén waves. *J. Geophys. Res.* **109**, A04205 (2004).
30. J. R. Wygant, A. Keiling, C. A. Cattell, R. L. Lysak, M. Temerin, F. S. Mozer, C. A. Kletzing, J. D. Scudder, V. Streltsov, W. Lotko, C. T. Russell, Evidence for kinetic Alfvén waves and parallel electron energization at 4–6 R_E altitudes in the plasma sheet boundary layer. *J. Geophys. Res.* **107**, SMP 24-1–SMP 24-15 (2002).
31. Y. Nishimura, T. Kikuchi, A. Shinbori, J. Wygant, Y. Tsuji, T. Hori, T. Ono, S. Fujita, T. Tanaka, Direct measurements of the Poynting flux associated with convection electric fields in the magnetosphere. *J. Geophys. Res.* **115**, A12212 (2010).
32. K. Stasiewicz, P. Bellan, C. Chaston, C. Kletzing, R. Lysak, J. Maggs, O. Pokhotelov, C. Seyler, P. Shukla, L. Stenflo, A. Streltsov, J.-E. Wahlund, Small-scale Alfvénic structure in the aurora. *Space Sci. Rev.* **92**, 423–533 (2000).
33. A. Keiling, J. R. Wygant, C. A. Cattell, F. S. Mozer, C. T. Russell, The global morphology of wave Poynting flux: Powering the aurora. *Science* **299**, 383–386 (2003).
34. C. C. Chaston, C. W. Carlson, J. P. McFadden, R. E. Ergun, R. J. Strangeway, How important are dispersive Alfvén waves for auroral particle acceleration? *Geophys. Res. Lett.* **34**, L07101 (2007).
35. P. T. Newell, T. Sotirelis, S. Wing, Diffuse, monoenergetic, and broadband aurora: The global precipitation budget. *J. Geophys. Res.* **114**, A09207 (2009).
36. J. Dombeck, C. Cattell, N. Prasad, E. Meeker, E. Hanson, J. McFadden, Identification of auroral electron precipitation mechanism combinations and their relationships to net downgoing energy and number flux. *J. Geophys. Res. Space Phys.* **123**, 10064–10089 (2018).
37. A. Keiling, G. K. Parks, J. R. Wygant, J. Dombeck, F. S. Mozer, C. T. Russell, A. V. Streltsov, W. Lotko, Some properties of Alfvén waves: Observations in the tail lobes and the plasma sheet boundary layer. *J. Geophys. Res.* **110**, A10511 (2005).
38. A. Keiling, J. R. Wygant, C. Cattell, W. Peria, G. Parks, M. Temerin, F. S. Mozer, C. T. Russell, C. A. Kletzing, Correlation of Alfvén wave Poynting flux in the plasma sheet at 4–7 R_E with ionospheric electron energy flux. *J. Geophys. Res.* **107**, SMP 24-1–SMP 24-13 (2002).
39. N. A. Tsyganenko, A model of the near magnetosphere with a dawn-dusk asymmetry 1. Mathematical structure. *J. Geophys. Res.* **107**, SMP 12-1–SMP 12-15 (2002).
40. N. A. Tsyganenko, A model of the near magnetosphere with a dawn-dusk asymmetry 2. Parameterization and fitting to observations. *J. Geophys. Res.* **107**, SMP 10-1–SMP 10-17 (2002).
41. N. C. Maynard, W. J. Burke, E. M. Basinska, G. M. Erickson, W. J. Hughes, H. J. Singer, A. G. Yahnin, D. A. Hardy, F. S. Mozer, Dynamics of the inner magnetosphere near times of substorm onsets. *J. Geophys. Res.* **101**, 7705–7736 (1996).
42. D. Schriver, M. Ashour-Abdalla, R. J. Strangeway, R. L. Richard, C. Kletzing, Y. Dotan, J. Wygant, FAST/Polar conjunction study of field-aligned auroral acceleration and corresponding magnetotail drivers. *J. Geophys. Res.* **108**, 8020 (2003).
43. P. K. Toivanen, D. N. Baker, W. K. Peterson, H. J. Singer, J. Watermann, J. R. Wygant, C. T. Russell, C. A. Kletzing, Polar observations of transverse magnetic pulsations initiated at substorm onset in the high-latitude plasma sheet. *J. Geophys. Res.* **108**, 1267 (2003).
44. A. V. Streltsov, W. Lotko, A. Keiling, J. R. Wygant, Numerical modeling of Alfvén waves observed by the Polar spacecraft in the nightside plasma sheet boundary layer. *J. Geophys. Res.* **107**, SMP 9-1–SMP 9-8 (2002).
45. A. V. Streltsov, W. Lotko, Reflection and absorption of Alfvénic power in the low-altitude magnetosphere. *J. Geophys. Res.* **108**, 8016 (2003).
46. C. C. Chaston, J. W. Bonnell, C. W. Carlson, J. P. McFadden, R. E. Ergun, R. J. Strangeway, Properties of small-scale Alfvén waves and accelerated electrons from FAST. *J. Geophys. Res.* **108**, 8003 (2003).
47. S. Wing, M. Gkioulidou, J. R. Johnson, P. T. Newell, C.-P. Wang, Auroral particle precipitation characterized by the substorm cycle. *J. Geophys. Res. Space Phys.* **118**, 1022–1039 (2013).
48. S. M. Hatch, C. C. Chaston, J. LaBelle, Alfvén wave-driven ionospheric mass outflow and electron precipitation during storms. *J. Geophys. Res. Space Phys.* **121**, 7828–7846 (2016).
49. S. M. Hatch, J. LaBelle, W. Lotko, C. C. Chaston, B. Zhang, IMF control of Alfvénic energy transport and deposition at high latitudes. *J. Geophys. Res. Space Phys.* **122**, 12189–12211 (2017).
50. B. Zhang, W. Lotko, O. Brambles, P. Damiano, M. Wiltberger, J. Lyon, Magnetotail origins of auroral Alfvénic power. *J. Geophys. Res.* **117**, A09205 (2012).
51. W. Lotko, Inductive magnetosphere–ionosphere coupling. *J. Atmos. Sol. Terr. Phys.* **66**, 1443–1456 (2004).
52. C. C. Chaston, C. Salem, J. W. Bonnell, C. W. Carlson, R. E. Ergun, R. J. Strangeway, J. P. McFadden, The turbulent Alfvénic aurora. *Phys. Rev. Lett.* **100**, 175003 (2008).
53. V. Génot, P. Louarn, F. Mottez, Alfvén wave interaction with inhomogeneous plasmas: Acceleration and energy cascade towards small-scales. *Ann. Geophys.* **22**, 2081–2096 (2004).
54. P. Song, C. T. Russell, R. J. Strangeway, J. R. Wygant, C. A. Cattell, R. J. Fitzenreiter, R. R. Anderson, Wave properties near the subsolar magnetopause: Pc 3–4 energy coupling for northward interplanetary magnetic field. *J. Geophys. Res.* **98**, 187–196 (1993).
55. L. Kepko, R. L. McPherron, O. Amm, S. Apatenkov, W. Baumjohann, J. Birn, M. Lester, R. Nakamura, T. I. Pulkkinen, V. Sergeev, Substorm current wedge revisited. *Space Sci. Rev.* **190**, 1–46 (2015).
56. T. Johansson, S. Figueiredo, T. Karlsson, G. Marklund, A. Fazakerley, S. Buchert, P.-A. Lindqvist, H. Nilsson, Intense high-altitude auroral electric fields – temporal and spatial characteristics. *Ann. Geophys.* **22**, 2485–2495 (2004).
57. R. L. Lysak, C. T. Dum, Dynamics of magnetosphere-ionosphere coupling including turbulent transport. *J. Geophys. Res.* **88**, 365–380 (1983).
58. D. J. Knudsen, M. C. Kelley, J. F. Vickrey, Alfvén waves in the auroral ionosphere: A numerical model compared with measurements. *J. Geophys. Res.* **97**, 77–90 (1992).
59. C. C. Chaston, J. W. Bonnell, L. Clausen, V. Angelopoulos, Energy transport by kinetic-scale electromagnetic waves in fast plasma sheet flows. *J. Geophys. Res.* **117**, A09202 (2012).
60. J. Vogt, Alfvén wave coupling in the auroral current circuit. *Surv. Geophys.* **23**, 335–377 (2002).

Acknowledgments

Funding: This research was supported by the NSF grant AGS-1613134 and the NASA grants NNX16AG67G and NNX10AL03G. **Author contributions:** A.K. conducted the majority of the data processing, analysis, and writing of this study. S.T. created Fig. 3 and assisted with the data interpretation. J.W. and J.D. provided the Polar data and assisted with the data interpretation. **Competing interests:** The authors declare that they have no competing interests. **Data and materials availability:** All data needed to evaluate the conclusions in the paper are present in the paper. The relevant Polar data may be obtained by request from the instrument principal investigators. The contact information for each principal investigator can be found at NASA’s archive (www-istp.gsfc.nasa.gov/istp/polar/principal_inv.html). The relevant Dst index can be downloaded from the World Data Center in Kyoto (<http://wdc.kugi.kyoto-u.ac.jp/aedir/>).

Submitted 24 October 2018

Accepted 16 May 2019

Published 26 June 2019

10.1126/sciadv.aav8411

Citation: A. Keiling, S. Thaller, J. Wygant, J. Dombeck, Assessing the global Alfvén wave power flow into and out of the auroral acceleration region during geomagnetic storms. *Sci. Adv.* **5**, eaav8411 (2019).